

CRONE Cruise Control System

Audrey Morand, Xavier Moreau, Pierre Melchior, Mathieu Moze, and Frank Guillemard

Abstract—This paper deals with vehicle longitudinal control performed by a cruise control (CC) system using the CRONE approach. A comparison between this approach, a classical proportional–integral (PI) controller, and an H-infini (Hinf) controller is presented. Simulations with these controllers are performed considering a complex vehicle model obtained from simulator software taking mass uncertainties, aerodynamic drag, gravity, and wind forces into account. This model also accounts for wheel dynamics with tire–road interactions that allow the analysis of the adherence effect. Results show better robustness to uncertainties with the second-generation CRONE controller, as already demonstrated with the CRONE suspension system and the CRONE ABS system.

Index Terms—CRONE controller, cruise control (CC) system, robustness analysis, vehicle dynamics.

I. INTRODUCTION

TRAFFIC safety is a major concern of automotive research with the aim of always reducing road casualties. In this context, “primary safety” refers to systems that prevent crashes [1], whereas “secondary safety” refers to systems that minimize the impact of a potential crash on new car occupants [2].

New vehicles tend to be equipped with more advanced driver assistance systems (ADAS) such as lane-keeping systems [3] or adaptive cruise control (ACC) [4]. Until now, cost was a limitation, and complex systems such as ACC were essentially implemented on premium vehicles. This will fade due to the evolutions of EuroNcap norms [5]. These kinds of features will progressively be mandatory to be awarded five stars. Recent surveys have shown that most car makers are working on autonomous vehicles [6].

Such systems have many advantages not only for safety but also for traffic fluency and for fuel consumption reduction. Some studies [7], [8] are looking to design new ADAS inspired by fishes, particularly their capacity to travel cooperatively in groups without collision and with no leader [9]. The behavior of each individual thus engenders a form of collective be-

Manuscript received March 17, 2014; revised August 4, 2014 and November 10, 2014; accepted December 13, 2014. Date of publication February 16, 2015; date of current version January 13, 2016. The review of this paper was coordinated by Prof. M. Benbouzid.

A. Morand is with the Laboratory IMS, UMR 5218 CNRS, University of Bordeaux, 33405 Talence, France and also with PSA Peugeot Citroën, 78943 Vélizy-Villacoublay, France (e-mail: audrey.morand@yahoo.fr).

X. Moreau and P. Melchior are with the Laboratory IMS, UMR 5218 CNRS, University of Bordeaux, 33405 Talence, France, and also with OpenLab PSA-IMS “Electronics and Systems for Automotive,” 33405 Talence, France (e-mail: xavier.moreau@ims-bordeaux.fr; pierre.melchior@ims-bordeaux.fr).

M. Moze and F. Guillemard are with PSA Peugeot Citroën, 78943 Vélizy-Villacoublay, France, and also with OpenLab PSA-IMS “Electronics and Systems for Automotive,” 33405 Talence, France (e-mail: Mathieu.moze@mps.com; franck.guillemard@mps.com).

Color versions of one or more of the figures in this paper are available online at <http://ieeexplore.ieee.org>.

Digital Object Identifier 10.1109/TVT.2015.2392074

havior promoting smoother travel and greater safety for all. The benefits linked to this type of individual assistance are shown to be greater safety, improved energy performance, and shorter travel time. The overall behavior of the shoal obtained through technology is suited to the road environment [10] by the following:

- avoiding collisions between vehicles and adapting to the road geometry;
- making the best use of the space available for efficient traffic management;
- minimizing travel time, emissions, and consumption by driving at an appropriate speed.

This fact (time gain) is presented in [11], which shows how the penetration of ACC contributes to driving time reduction.

In this paper, focus is made on longitudinal control performed by a CC system that regulates speed of the vehicle around a reference given by the driver or of a more complex system ahead.

In [12], a very simple vehicle model without the wheel dynamics is presented. However, most of the previous works [13]–[15] on longitudinal control were based on simpler models neglecting important nonlinear aspects of vehicle such as load variation, rolling resistance, and road adherence effects. Here, the model used is more complex, and it accounts for wheel dynamics with tire–road interaction that allow the analysis of the adherence effect.

Different control strategies can easily be found in literature [13], including fuzzy logic, gain scheduling control involving proportional–integral–derivative controllers [14], and sliding-mode control [15]. The method presented in this paper is based on a CRONE control strategy, which is already known for its applications in [16]–[28] but never applied to CC systems. Results are compared to those obtained using a classical proportional–integral (PI) controller because of its wide acceptance across industries and to those obtained using an H-infini (Hinf) controller for its robustness property.

This paper is given as follows. After this introduction, Section II presents the context. Section III gives a nonlinear model used for analysis of vehicle dynamic behavior from which a linearized model is deduced for CC design in the frequency domain. Section IV deals with the design of the PI, Hinf, and CRONE controllers, whereas Section V provides a robustness analysis of the stability degree and the simulation results. Finally, conclusion and prospects are presented in Section VI.

II. PROBLEM FORMULATION

The car CC system design is considered here. The road is assumed straight and with no overtaking possibility, meaning



Fig. 1. Active wheel from Michelin.



Fig. 2. Driving simulator.

the vehicles can only drive on one lane. These assumptions are made for the focus on longitudinal dynamics only. The vehicle of interest is a small car designed particularly for urban environment. It can take only two persons, including the driver. This electrical car is motorized by two in-wheel 30-kW motors, similar to the one presented in Fig. 1, in front wheels only [29].

The vehicle is equipped with a CC system that the driver can activate with a target velocity from 30 to 110 km/h. Different cases are presented to compare performance of a CRONE controller and a PI one. The driver activates the CC system at a certain velocity, which is called velocity target in the following, and the vehicle should follow the speed, even when confronted to a wind gust and/or a nonflat road. This study seeks to establish a vehicle model, including wheel dynamics, to obtain a cruise controller taking into account any parameter variations. An important care is thus brought to the sensibility analysis.

III. SYSTEM MODELING

As the cruise controller is part of a more complex ADAS that will be tested on a driving simulator (see Fig. 2), the final model used for this application will be the one from the simulator software SCANr Studio. This simulator is acknowledged to be realistic and to reflect real-life driving situations for both the driver and the vehicle. Feelings of driving are achieved by a

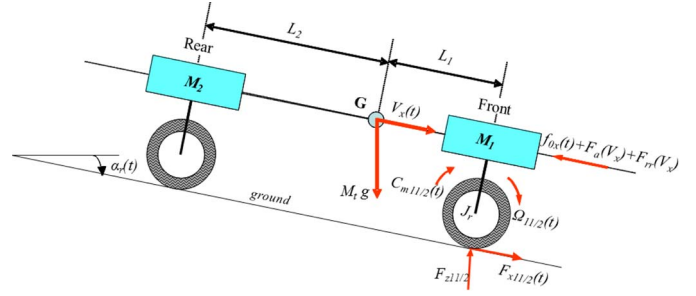


Fig. 3. Vehicle notation.

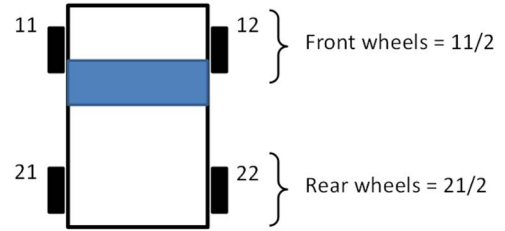


Fig. 4. Wheel notation.

real driver's cab moving with six jacks along rails of 10 m in longitude and 15 m in latitude.

Here, the vehicle model is described. This model is not linear and is used for validation purposes only. Some simplifications are thus made in a second time to obtain a linear model that is used for controller design.

Remark: Regarding all physical quantities, the following notation is adopted in this paper:

$$X(t) = X^e + x(t) \quad (1)$$

where $X(t)$ is the value of the physical quantity, in an absolute referential; X^e is defined as the reference (constant) value fixed by the steady-state operation around which dynamical behavior is studied; and $x(t)$ represents the small variations of $X(t)$ around its equilibrium value X^e . In short, all notations in small letter are variations, and all physical quantities without capital notation are quantities with a zero reference.

In this framework, the Laplace transform of variation $x(t)$ is written as $\tilde{X}(s) = Lt\{x(t)\}$.

A. Vehicle Model

For the purpose of this analysis where the focus is done on longitudinal dynamics, the vehicle representation is the single-track one also known as bicycle model. In this approach, the forces applied on the vehicle along with its geometric parameters are shown in Fig. 3 [30].

Regarding only longitudinal speed, lateral dynamics are neglected. This model includes longitudinal components of aerodynamic drag F_a , rolling resistance F_{rr} , and gravity and wind forces f_{0x} . Longitudinal dynamics can be described by Newton's second law, i.e.,

$$M_t \dot{V}_x(t) = F_{\sum x}(t) - F_g(t) - f_{0x}(t) - F_a(V_x) - F_{rr}(V_x) \quad (2)$$

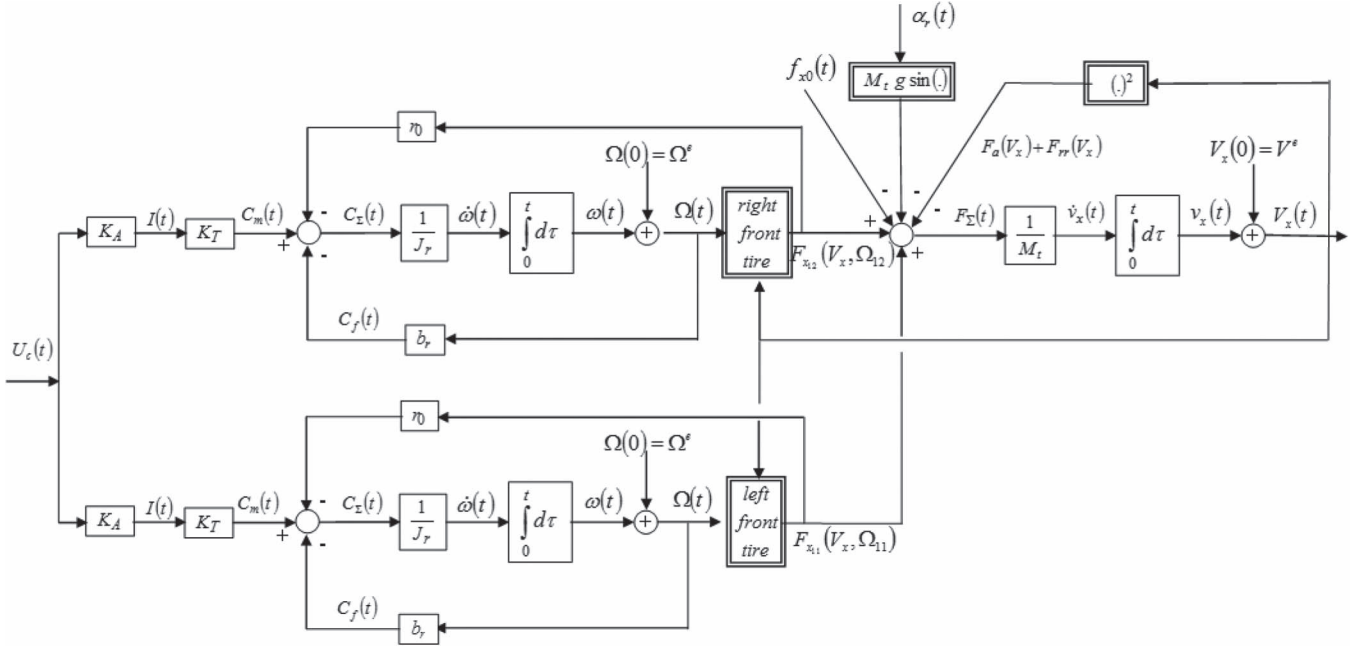


Fig. 5. Block diagram of the validation model.

with

$$F_{\sum x}(t) = F_{x11}(t) + F_{x12}(t) + F_{x21}(t) + F_{x22}(t) \quad (3)$$

where each F_{xij} is, respectively, each pneumatic tangential force to the road. For clarity, indexes are defined for each wheel as a matrix, as shown in Fig. 4.

M_t is the vehicle mass, $f_{x0}(t)$ is the longitudinal wind force applied at the gravity center, $F_g(t)$ is the gravity-induced force according to the road slope $\alpha_r(t)$

$$F_g(t) = M_t g \sin \alpha_r(t) \quad (4)$$

$F_a(V_x)$ is the aerodynamic drag force according to the longitudinal velocity V_x

$$F_a(V_x) = \frac{1}{2} \rho S_x C_{xx} V_x^2(t) \quad (5)$$

in which ρ is the air density, C_{xx} is the aerodynamic drag coefficient, S_x is the frontal area of the vehicle, and $F_{rr}(V_x)$ is the resultant force of the rolling resistance from the four wheels expressed in the center of gravity, i.e.,

$$F_{rr}(V_x) = (\lambda_0 + \lambda_2 V_x^2(t)) M_t g \quad (6)$$

with λ_0 and λ_2 being positive constants.

Vehicle motion is generated by forces applied at the wheel-road contacts considered as points. In the special case of this study, the absence of torque applied at the rear wheels leads to negligible forces for $F_{x21}(t)$ and $F_{x22}(t)$, hence leading to the following simplification: $F_{\sum x}(t) = F_{x11}(t) + F_{x12}(t)$.

Front-wheel dynamics are described as follows:

$$\begin{cases} J_r \dot{\Omega}_{11}(t) = C_{m11}(t) - r_0 F_{x11}(t) - C_{f11}(t) \\ J_r \dot{\Omega}_{12}(t) = C_{m12}(t) - r_0 F_{x12}(t) - C_{f12}(t) \end{cases} \quad (7)$$

where J_r is the wheel inertia, r_0 is the wheel radius, $\Omega_{11/2}(t)$ is the angular velocities of wheels, $C_{m11/2}(t)$ is the torque applied by the motors at the front wheels, and $C_{f11/2}(t)$ is the viscous friction torque, respectively, applied at each wheel, i.e.,

$$C_{f11/2}(t) = b_r \Omega_{11/2}(t) \quad (8)$$

where b_r is the viscous friction coefficient.

Note that longitudinal efforts $F_{x11}(t)$ and $F_{x12}(t)$ can be deduced using the tire model created by Pacejka and Besselink [31], which takes into account road adherence coefficient μ and slip ratio $T_{11/2}(V_x(t), \Omega_{11/2}(t))$, namely

$$F_{x11/2}(t) = \mu D_x \sin \left[C_x \arctan \left(B_x \left[(1 - E_x) T_{11/2}(t) + \frac{E_x}{B_x} \arctan \left(B_x T_{11/2}(t) \right) \right] \right) \right] \quad (9)$$

where macroparameters B_x , C_x , D_x , and E_x depend on microparameters and on the vertical load F_z on each axle. Moreover, road adherence coefficient μ is considered an uncertain parameter between 0.4 (slippery road) and 1 (dry road), considered equal for both wheels. In the same way, vertical load F_{zij} is also an uncertain parameter that equals to the load located at each wheel. The uncertainty comes from the vehicle mass that varies between loaded and unloaded vehicles. Thus, considering symmetrical load on front wheels, F_z is given as follows:

$$F_{z11} = F_{z12} = \frac{M_1}{2} g \cos \alpha_r. \quad (10)$$

Motors are brushless, and their dynamics are considered to follow those of a direct current motor. Neglecting the dynamics of the voltage current amplifier, voltage command, current, and torque are thus given by

$$I(t) = K_A U_c(t) \quad \text{and} \quad C_{m11/2}(t) = K_T I(t) \quad (11)$$

TABLE I
MODEL PARAMETERS

M_t	600 to 900 Kg	C_{xx}	0.5
g	10 m/s ²	b_r	10 ⁻³ Nm.s/rad
ρ	1.225 Kg/m ³	J_r	1 Kg.m ²
S_x	2 m ²	K_T	25 Nm/A
r_θ	0.3 m	K_A	1 A/V

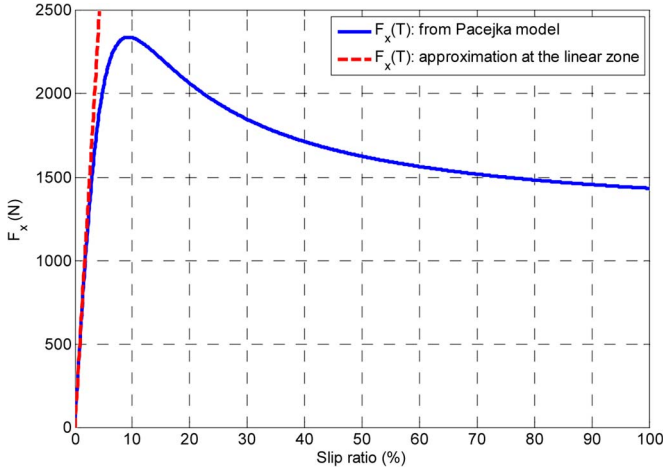


Fig. 6. Characteristics F_x with respect to the slip ratio.

where K_A is the voltage-to-current amplifier gain, and K_T is the constant torque associated with each motor.

Note that the hypothesis of symmetrical load with identical motors assumed in this study is that the commands are equal for both motors. In this framework, Fig. 5 describes the vehicle from in-wheel motor control voltage to longitudinal speed.

Simulations show that applying a step of the maximum voltage command (11.8 V) with the parameters presented in Table I leads to $V_x(t)$ passing from 0 to 100 km/h in 9 s. This behavior is representative of these kinds of vehicles. This model is the one used in the following parts, unless otherwise stated.

B. Linear Model Used for Frequency-Domain Controller Design

To exploit the time–frequency duality and thus to use a frequency-domain control-system design, the preceding model is linearized around operating points.

- Slip ratio $T_{11/2}^e(V_x^e, \Omega_{11/2}^e)$ varies around the equilibrium point between $[-5\%; 5\%]$, staying in the linear operating area, as shown by the characteristic function of F_x with respect to T of the Pacejka model in Fig. 6.

Longitudinal forces are thus written as

$$F_{\frac{x11}{2}}(t) = F_{\frac{x11}{2}}^e + f_{\frac{x11}{2}}(t) \quad (12)$$

where

$$F_{\frac{x11}{2}}^e = c_{\frac{x11}{2}} T_{\frac{11}{2}}^e \quad (13)$$

and

$$f_{\frac{x11}{2}}(t) = c_{\frac{x11}{2}} \tau_{\frac{11}{2}}(t) \quad (14)$$

with $T_{11/2}(t) = T_{11/2}^e + \tau_{11/2}(t)$ and c_x coming from the Pacejka formula applied for each tire in which B_x , C_x , D_x , and E_x are expressed according to the vertical load F_z (numerical indexes are deleted for clarity)

$$c_x = \left. \frac{\partial F_x}{\partial T} \right|_{T=T^e} \quad (15)$$

and in the particular case of the linear operating area

$$c_x = \mu B_x C_x D_x. \quad (16)$$

- Slip ratio needs to be linearized. First-order Taylor series expansion gives for the driving phase (index d)

$$T_d(V_x(t), \Omega(t)) \approx T_d^e + \eta_d \omega(t) + \mu_d v_x(t) \quad (17)$$

with

$$T_d^e = 1 - \frac{V_x^e}{r_0 \Omega^e} \geq 0 \quad (18)$$

$$\eta_d = \left. \frac{\partial T_d}{\partial \Omega} \right|_{V_x=V_x^e, \Omega=\Omega^e} = \frac{V_x^e}{r_0 \Omega^{e2}} = cste > 0 \quad (19)$$

and

$$\mu_d = \left. \frac{\partial T_d}{\partial V_x} \right|_{V_x=V_x^e, \Omega=\Omega^e} = -\frac{1}{r_0 \Omega^e} = cste < 0. \quad (20)$$

- The aerodynamic force is then linearized around the reference velocity fixed by the driver as follows:

$$F_a(V_x(t)) \approx F_a^e + b_a v_x(t) \quad (21)$$

with

$$\begin{cases} F_a^e = \frac{1}{2} \rho S_x C_x V_x^{e2} \\ b_a = \left. \frac{\partial F_a}{\partial V_x} \right|_{V_x=V_x^e} = \rho S_x C_x V_x^e. \end{cases} \quad (22)$$

- In the same way, rolling resistance is linearized as follows:

$$F_{rr}(V_x(t)) \approx F_{rr}^e + b_{rr} v_x(t) \quad (23)$$

with

$$\begin{cases} F_{rr}^e = (\lambda_0 + \lambda_2 V_x^{e2}) M_t g \\ b_{rr} = \left. \frac{\partial F_{rr}}{\partial V_x} \right|_{V_x=V_x^e} = 2\lambda_2 M_t g V_x^e. \end{cases} \quad (24)$$

- Moreover, considering the road slope is limited to small angles, we have

$$\sin \alpha_r(t) \approx \alpha_r(t). \quad (25)$$

A state-space representation of this linear model can be established, namely

$$\begin{cases} \dot{\underline{x}} = A\underline{x} + B\underline{u} \\ y = C\underline{x} + D\underline{u} \end{cases} \quad (26)$$

where

$$\underline{x} = \begin{pmatrix} x_1(t) = v_x(t) \\ x_2(t) = \omega_r(t) \end{pmatrix}, \quad \underline{u} = \begin{pmatrix} u_1(t) = \alpha_r(t) \\ u_2(t) = f_{0x}(t) \\ u_3(t) = u_c(t) \end{pmatrix}, \quad y = v_x(t) \quad (27)$$

$$A = \begin{bmatrix} a_{11} = \frac{2c_x\mu_d - b_a - b_{rr}}{M_t} & a_{12} = \frac{2c_x\eta_d}{M_t} \\ a_{21} = \frac{-r_0c_x\mu_d}{J_r} & a_{22} = \frac{-r_0c_x\eta_d - b_r}{J_r} \end{bmatrix}$$

$$B = \begin{bmatrix} -g & \frac{-1}{M_t} & 0 \\ 0 & 0 & \frac{K_A K_T}{J_r} \end{bmatrix}, \quad C = \begin{bmatrix} 1 & 0 \end{bmatrix}, \quad D = 0. \quad (28)$$

The transfer matrix H is thus given as follows:

$$H = C[sI - A]^{-1}B + D = \begin{bmatrix} H_{11}(s) & H_{12}(s) & H_{13}(s) \end{bmatrix} \quad (29)$$

where

$$H_{11}(s) = \left. \frac{\tilde{V}_x(s)}{\tilde{\alpha}_r(s)} \right|_{\substack{f_{0x}=0 \\ u_c=0}}, \quad H_{12}(s) = \left. \frac{\tilde{V}_x(s)}{\tilde{F}_{0x}(s)} \right|_{\substack{\alpha_r=0 \\ u_c=0}}$$

$$H_{13}(s) = \left. \frac{\tilde{V}_x(s)}{\tilde{U}_c(s)} \right|_{\substack{\alpha_r=0 \\ f_{0x}=0}} \quad (30)$$

and the characteristic polynomial $P(s) = \det[sI - A]$ by

$$P(s) = s^2 + \alpha s + \beta, \quad \text{with} \quad \begin{cases} \alpha = -(a_{11} + a_{22}) > 0 \\ \beta = a_{11}a_{22} - a_{12}a_{21} > 0. \end{cases} \quad (31)$$

A numerical analysis shows that $P(s)$ has two negative distinct real roots ω_1 and ω_2 ; hence, $P(s)$ can be rewritten in the following form:

$$P(s) = (s + \omega_1)(s + \omega_2), \quad \text{with} \quad \begin{cases} \omega_1 + \omega_2 = \alpha \\ \omega_1\omega_2 = \beta. \end{cases} \quad (32)$$

Numerical and analytical analyses of α and β show that ω_1 and ω_2 can be approximated by

$$\begin{cases} \omega_1 = f(V_x^e, M_t) \approx \frac{b_r}{M_t} \\ \omega_2 = g(V_x^e, M_t, \mu) \approx \frac{r_0c_x\eta_d}{J_r} \end{cases}, \quad \text{with} \quad \omega_2 \gg \omega_1. \quad (33)$$

ω_1 is thus associated with a slow mode (vehicle dynamics for longitudinal translation), and ω_2 is associated with a fast mode (rotation of wheel dynamics).

C. System Uncertainties

Transfer function $H_{13}(s)$ used for frequency-domain design methodology of feedback system is given as follows:

$$H_{13}(s) = \left. \frac{\tilde{V}_x(s)}{\tilde{U}_c(s)} \right|_{\substack{\alpha_r=0 \\ f_{0x}=0}} = \frac{G_0}{\left(\frac{s}{\omega_1} + 1\right)\left(\frac{s}{\omega_2} + 1\right)} \quad (34)$$

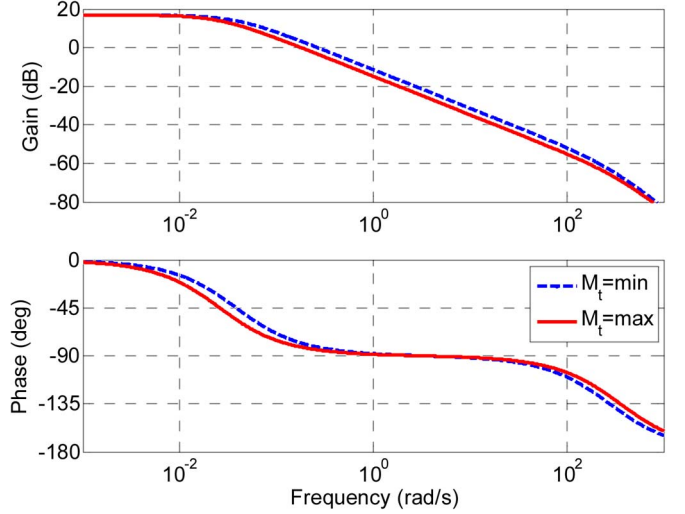


Fig. 7. Sensibility to mass variation.

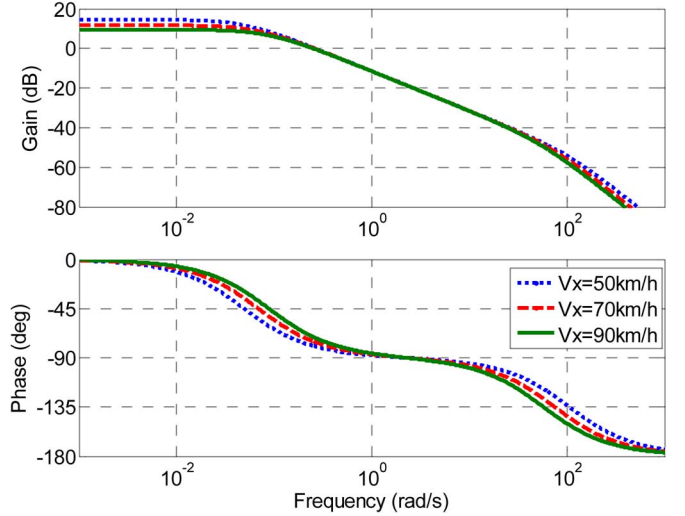


Fig. 8. Sensibility to target velocity variation.

where

$$G_0 = h(V_x^e) \approx \frac{2K_A K_T}{r_0 b_a}. \quad (35)$$

The numerical values of G_0 , ω_1 , and ω_2 depend on the operating point. Uncertainties in the vehicle model are associated to mass M_t , reference velocity V_{xref} , and adherence μ of road. In this paper, those parameters are considered to be bounded according to

$$\begin{cases} 30 \text{ km/h} < V_{xref} < 110 \text{ km/h} \\ 600 \text{ kg} < M_t < 900 \text{ kg} \\ 0.4 < \mu < 1. \end{cases} \quad (36)$$

D. Sensibility Analysis

The sensibility to the uncertain parameters is observed from the frequency response $H_{13}(j\omega)$. Figs. 7–9 present the

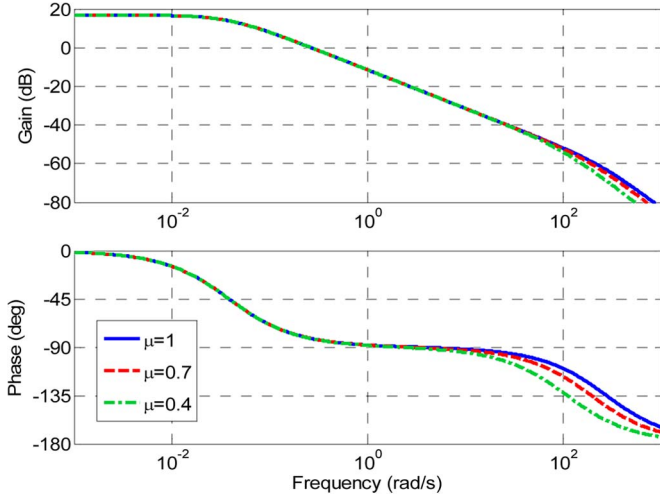


Fig. 9. Sensibility to road adherence variation.

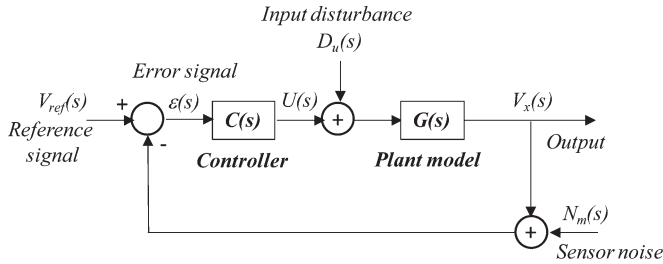


Fig. 10. Closed-loop system diagram for controller synthesis.

sensibility with respect to mass variation, reference velocity variation, and road adherence variation, respectively. To summarize, the observed results are in accordance with (33) and (35), which are given in the following.

- The mass variation leads to variations of ω_1 and ω_2 (Fig. 7).
- The reference velocity variation leads to variations of G_0 , ω_1 , and ω_2 (see Fig. 8).
- The road adherence variation leads to variation of ω_2 (see Fig. 9).

Furthermore, we can observe the dynamic decoupling between the two modes.

IV. FREQUENCY-DOMAIN CONTROLLER DESIGN

To obtain a significant comparison between PI and CRONE controllers, the same rapidity and stability degree are chosen. The specifications are defined for the general case in the first place. Then, considering the nominal operating point chosen as minimum mass (600 kg), the median value for the target velocity (70 km/h), and the adherence coefficient of 1, those specifications are translated into constraints assigned to each controller design. Fig. 10 presents the diagram used for control design where $G(s) = H_{13}(s)$.

Functional equations associated with Fig. 10 are as follows:

- output:

$$\tilde{V}_x(s) = -T(s)N_m(s) + GS(s)D_u(s) + T(s)\tilde{V}_{\text{ref}}(s) \quad (37)$$

- error:

$$\varepsilon(s) = -S(s)N_m(s) - GS(s)D_u(s) + S(s)\tilde{V}_{\text{ref}}(s) \quad (38)$$

- control effort:

$$\tilde{U}(s) = -CS(s)N_m(s) - T(s)D_u(s) + CS(s)\tilde{V}_{\text{ref}}(s) \quad (39)$$

$$\text{with } \begin{cases} S(s) = 1/(1 + \beta(s)) : & \text{sensitivity function} \\ T(s) = 1 - S(s) : & \text{complementary sensitivity function} \\ GS(s) = G(s)S(s) : & \text{input disturbance sensitivity function} \\ CS(s) = C(s)S(s) : & \text{input sensitivity function} \\ \beta(s) = C(s)G(s) : & \text{open-loop transfer function.} \end{cases}$$

A. Performance Specifications

The performance specifications concern the following:

- the stability degree;
- the bandwidth;
- the precision in steady state;
- the rejection level of the measurement noise;
- the rejection level of the input perturbation;
- the plant input sensitivity.

In the following, the study is performed in the frequency domain. The **stability degree** can be specified with respect to module margin M_M , gain margin M_G , or phase margin M_Φ . The last one is used in this paper and is given as

$$M_\Phi = \pi + \arg \beta(j\omega_u) \quad (40)$$

where ω_u is the open-loop crossover frequency defined such that

$$|\beta(j\omega_u)| = 1. \quad (41)$$

The stability degree specification is thus encompassed within the following constraint:

$$M_\Phi \geq M_{\Phi_{\min}} \quad (42)$$

where $M_{\Phi_{\min}}$ represents the minimal acceptable value of the phase margin. Substituting M_Φ from (42) in (40) leads the constraint of the open-loop argument for the crossover frequency ω_u to be computed as

$$\arg \beta(j\omega_u) \geq -\pi + M_{\Phi_{\min}}. \quad (43)$$

The argument of the controller can then be deduced for (43) with respect to

$$\arg \beta(j\omega) = \arg C(j\omega) + \arg G(j\omega) \quad (44)$$

where $G(s)$ represents the plant transfer function. Hence, the reduced form of the controller argument constraint at the crossover frequency is

$$\arg C(j\omega_u) \geq -\pi + M_{\Phi_{\min}} - \arg G(j\omega_u). \quad (45)$$

The bandwidth specification is also computed to impose the crossover frequency ω_u . The aim of this constraint is to fix the closed-loop dynamics. The frequency range that is concerned by this condition is

$$\omega_u \leq \omega_{u\max} \quad (46)$$

where $\omega_{u\max}$ represents the maximal acceptable value of ω_u . Referring to (41) and knowing that

$$|\beta(j\omega)| = |C(j\omega)| |G(j\omega)| \quad (47)$$

a controller gain constraint at the open-loop crossover frequency ω_u can be deduced from (46) as follows:

$$|C(j\omega_u)| \leq |G(j\omega_{u\max})|^{-1}. \quad (48)$$

Concerning the **rejection level of the measurement noise**, it is calculated using a specification applied to the complementary sensitivity function module as follows:

$$\forall \omega \geq \omega_T, \quad |T(j\omega)| = |\beta(j\omega)| |1 + \beta(j\omega)|^{-1} \leq A \quad (49)$$

where A imposes the desired rejection noise level for a given frequency ω_T , i.e.,

$$|T(j\omega_T)| = A. \quad (50)$$

If the value ω_T is chosen to be much bigger than ω_u , (49) can be rewritten as

$$\forall \omega \geq \omega_T \gg \omega_u, \quad |T(j\omega)| \approx |\beta(j\omega)| \leq A. \quad (51)$$

Hence, a new controller gain constraint around the frequency ω_T is deduced by combining (51) and (47) as follows:

$$\forall \omega \geq \omega_T \gg \omega_u, \quad |C(j\omega)| \leq A |G(j\omega_T)|^{-1}. \quad (52)$$

The **rejection level of the input disturbance** is used for low frequencies and is computed using a specification as follows:

$$\forall \omega \leq \omega_{GS}, \quad |GS(j\omega)| = |G(j\omega)| |1 + \beta(j\omega)|^{-1} \leq B \quad (53)$$

where B represents the desired rejected input disturbance level for a frequency ω_{GS}

$$|GS(j\omega_{GS})| = B. \quad (54)$$

When choosing $\omega_{GS} \ll \omega_u$, (53) can be written as follows:

$$\forall \omega \leq \omega_{GS} \ll \omega_u, \quad |GS(j\omega)| \approx |C(j\omega)|^{-1} \leq B. \quad (55)$$

Hence, a new controller gain constraint around the frequency ω_{GS} is deduced from (55) as follows:

$$\forall \omega \leq \omega_{GS} \ll \omega_u, \quad |C(j\omega)| \geq B^{-1}. \quad (56)$$

The plant input sensitivity is computed using a specification of the following form:

$$\forall \omega \geq \omega_{CS}, \quad |CS(j\omega)| = |C(j\omega)(1 + \beta(j\omega))^{-1}| \leq D \quad (57)$$

where D represents the desired maximal value at a frequency ω_{CS} , i.e.,

$$|CS(j\omega_{CS})| = D. \quad (58)$$

If the frequency ω_{CS} is much bigger than ω_u , (57) can be rewritten as

$$\forall \omega \geq \omega_{CS} \gg \omega_u, \quad |C(j\omega)| \leq D. \quad (59)$$

The constraints (52) and (59) represent the same aspect, which is the controller gain at high frequencies. Hence, they can be reduced to one constraint by choosing the lowest value of these two relations. Thus

$$\forall \omega \gg \omega_u, \quad |C(j\omega)| \leq \min \left[A |G(j\omega_T)|^{-1}, D \right]. \quad (60)$$

B. User Constraints

Once the uncertain model transfer function is defined, the user constraints for the design of the three controllers are presented here.

- Stability degree: $M_{\Phi_{\min}} = 45^\circ \Leftrightarrow Q_{T\max} = 3$ dB, where $Q_{T\max}$ is the maximum of the complementary sensitivity function (resonance peak).
- Rejection level of the measurement noise:

$$\forall \omega \geq \omega_T = 10\omega_u, \quad |T(j\omega)|_{\text{dB}} \leq A_{\text{dB}} = -20 \text{ dB}.$$

- Rejection level of the input perturbation:

$$\forall \omega \leq \omega_{GS} = 0.1\omega_u, \quad |GS(j\omega)|_{\text{dB}} \leq B_{\text{dB}} = -20 \text{ dB}.$$

- Plant input sensitivity:

$$\forall \omega \geq \omega_{CS} = 10\omega_u, \quad |CS(j\omega)|_{\text{dB}} \leq D_{\text{dB}} = 10 \text{ dB}.$$

C. PI Controller

The PI transfer function is given by

$$C_{\text{PI}}(s) = C_{0\text{PI}} \left(\frac{\left(1 + \frac{s}{\omega_i}\right)}{\left(\frac{s}{\omega_i}\right)} \right) \quad (61)$$

where ω_i is the transitional frequency, and $C_{0\text{PI}}$ is a positive constant.

To compute the PI transfer function directly according to the specifications, parameter b , i.e.,

$$b = \frac{\omega_u}{\omega_i} \quad (62)$$

is inserted in (61), leading to the following PI function:

$$C_{\text{PI}}(s) = C_{0\text{PI}} \left(\frac{1 + bs/\omega_u}{\frac{bs}{\omega_u}} \right). \quad (63)$$

Hence, the PI module and phase are given by

$$\begin{cases} |C_{PI}(j\omega)| = \frac{C_{0PI} \sqrt{1 + \left(\frac{b\omega}{\omega_u}\right)^2}}{\left(\frac{b\omega}{\omega_u}\right)} \\ \arg C_{PI}(j\omega) = \arctan\left(\frac{b\omega}{\omega_u}\right) - \pi/2. \end{cases} \quad (64)$$

At the open-loop crossover frequency ω_u , (64) can thus be rewritten as

$$\begin{cases} C_{PI_u} = |C_{PI}(j\omega_u)| = C_{0PI} \sqrt{1 + b^2}/b \\ \phi_{PI_u} = \arg C_{PI}(j\omega_u) = \arctan(b) - \pi/2. \end{cases} \quad (65)$$

At low frequencies ($\omega \ll \omega_u$), (64) gives

$$\forall \omega \ll \omega_u, |C_{PI}(j\omega)| \approx C_{0PI} \left(\frac{\omega_u}{(b\omega)} \right) \text{ and } \arg C(j\omega) \approx -\pi/2 \quad (66)$$

and at high frequencies ($\omega \gg \omega_u$)

$$\forall \omega \gg \omega_u, |C_{PI}(j\omega)| \approx C_{0PI} \text{ and } \arg C_{PI}(j\omega) \approx 0. \quad (67)$$

Considering system (64) and the nominal plant, the constraints of (45), (48), (52), (56), and (59), valid independently of the controller nature, can be rewritten to best suit the PI controller as

$$\arctan(b) - \pi/2 \geq -\pi + M_{\Phi_{\min}} - \arg G(j\omega_{u \max}) \quad (68)$$

$$C_{0PI} \sqrt{1 + b^2}/b \geq |G(j\omega_{u \max})|^{-1}. \quad (69)$$

$$\forall \omega \geq \omega_T \gg \omega_u, C_{0PI} \leq A |G(j\omega_T)|^{-1} \quad (70)$$

$$\forall \omega \leq \omega_{GS} \ll \omega_u, C_{0PI} \left(\frac{\omega_{u \max}}{(b\omega)} \right) \geq B^{-1} \quad (71)$$

and

$$\forall \omega \gg \omega_{CS} \gg \omega_u, C_{0PI} \leq D. \quad (72)$$

The next step consists in applying the user constraints in the preceding relations to determine the optimal values of b , C_{0PI} , and $\omega_{u \max}$.

– From relation (72), we have

$$\max[C_{0PI}] = D \Rightarrow C_{0PI} = 3.16 \text{ Vs/m}. \quad (73)$$

– From relation (70), we have

$$\begin{aligned} |G(j\omega_T)| &= |G(j10\omega_u)| \leq \frac{A}{C_{0PI}} \\ \Rightarrow |G(j10\omega_u)|_{\text{dB}} &\leq -30 \text{ dB} \\ \Rightarrow 10\omega_u &= 10 \text{ rad/s} \Rightarrow \omega_{u \max} = 1 \text{ rad/s}. \end{aligned} \quad (74)$$

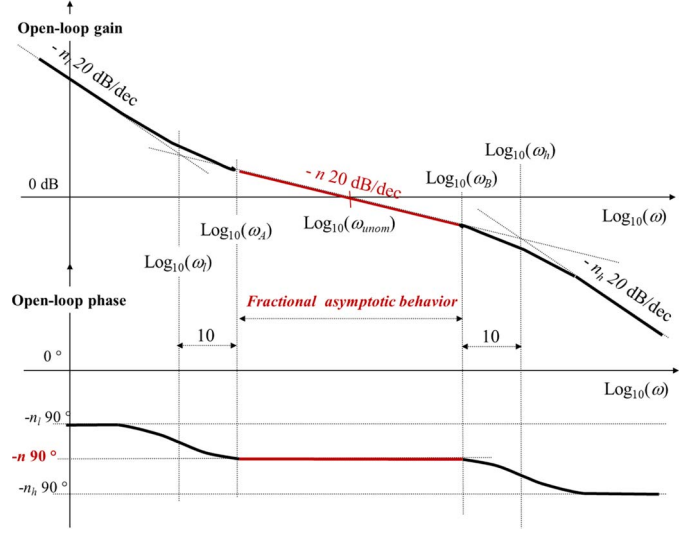


Fig. 11. Loop shaping method.

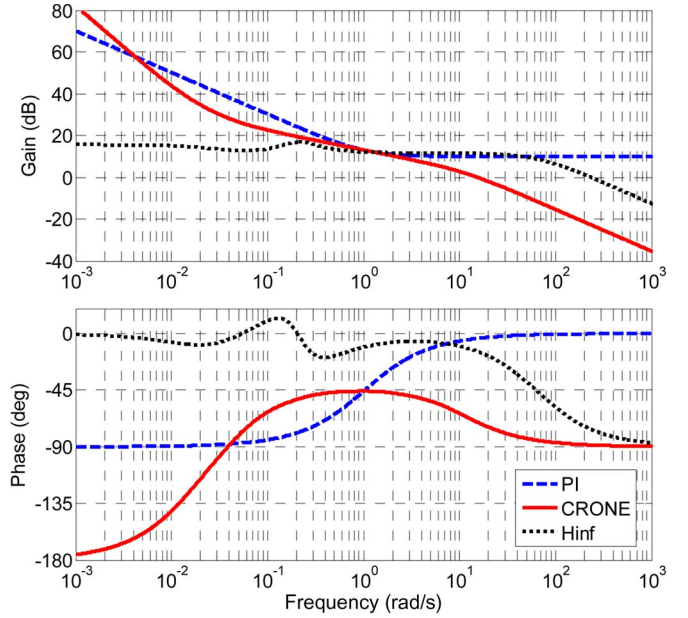


Fig. 12. Bode plots of the PI (in blue), the Hinf (in black), and the CRONE (in red) controllers.

– From relation (68), we have

$$\begin{aligned} b &\geq \tan \left[M_{\Phi_{\min}} - \frac{\pi}{2} - \arg G(j\omega_{u \max}) \right] = 0.933 \\ \Rightarrow b &= 1 \Rightarrow \omega_i = \frac{\omega_{u \max}}{b} = 1 \text{ rad/s}. \end{aligned} \quad (75)$$

D. Hinf Controller

The synthesis of the Hinf controller is made with mixed sensitivity from the user constraints on $S(j\omega)$, $CS(j\omega)$, $T(j\omega)$, and $GS(j\omega)$. The results obtained with this controller are shown in the performance analysis (see Section V).

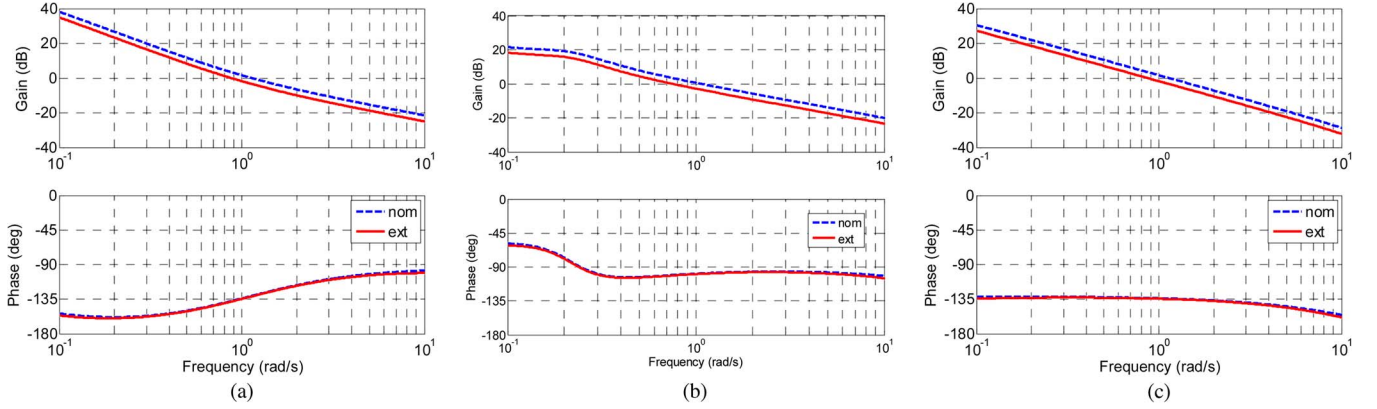


Fig. 13. Open-loop Bode plots for the (a) PI controller, the (b) Hinf controller, and the (c) CRONE controller.

E. CRONE Controller

Three generations of CRONE control are available [32]–[36]. The fact that the specified crossover frequency ω_u is not in a constant phase frequency range implies the use of the second generation. This controller can ensure robustness when plant reparametrization leads only to gain variation around ω_u .

The second-generation CRONE approach is based on a regulator design from the open-loop constraints (robust loop shaping) [37]. For second generation, the open-loop transfer function is

$$\beta(s) = K_0 \left(\frac{1 + \frac{s}{\omega_l}}{\frac{s}{\omega_l}} \right)^{n_l} \left(\frac{1 + \frac{s}{\omega_h}}{1 + \frac{s}{\omega_l}} \right)^n \frac{1}{\left(1 + \frac{s}{\omega_h} \right)^{n_h}} \quad (76)$$

where K_0 is a gain; ω_l and ω_h are the transitional low and high frequencies, respectively; n_l is the order at low frequencies; n is the order around crossover frequency ω_u ; and n_h is the order at high frequencies. CRONE controller design is then associated to determination of optimal values of these parameters. Optimality is achieved through minimization of a criterion defining performance robustness in the case of nominal plant reparametrization [38]. The nominal open-loop transfer function is denoted $\beta_0(s)$ and is modeled using the loop shaping method (see Fig. 11).

The frequency response $C_{\text{crone}}(j\omega)$ of the fractional controller is obtained from the nominal open-loop frequency response $\beta_0(j\omega)$ and the nominal plant frequency response $G_0(j\omega)$, namely

$$C_{\text{crone}}(j\omega) = \beta_0(j\omega)G_0^{-1}(j\omega). \quad (77)$$

Fractional order n is calculated by taking into account the phase margin M_Φ and the phase $(-n \cdot 90^\circ)$ of the open loop around ω_u

$$n = \frac{-(-180 + M_\Phi)}{90} = 1.5. \quad (78)$$

The synthesis of the rational controller that can be implemented consists in identifying the frequency response of $C_{\text{crone}}(j\omega)$ by the one of a rational transfer function $C_{\text{rat}}(j\omega)$ [39]. Using $n_l = 2$, $n_h = 3$ to meet the steady state specifica-

tions considering the plant asymptotic behavior at low and high frequencies and $n = 1.5$, the frequency response becomes

$$C_{\text{rat}}(j\omega) = C_0 \left(\frac{\omega_l}{j\omega} \right)^2 \frac{\left(1 + \frac{j\omega}{\omega_{1,\text{nom}}} \right) \left(1 + \frac{j\omega}{\omega_{2,\text{nom}}} \right)}{\left(1 + \frac{j\omega}{\omega_h} \right)} \prod_{i=1}^N \left(\frac{1 + \frac{j\omega}{\omega'_i}}{1 + \frac{j\omega}{\omega_i}} \right) \quad (79)$$

where

$$C_0 = \frac{K_0}{G_{0,\text{nom}}} \quad (80)$$

and the last product is the approximation of the noninteger part as defined in [40]. In this case, $N = 4$ is sufficient to obtain adequate performances. Finally, the numerical parameter values are

$$\begin{aligned} C_0 &= 6.798 \text{ V} \cdot \text{s/m} \\ \omega_l &= 0.0437 \text{ rad/s}, \quad \omega'_1 = 0.0599 \text{ rad/s}, \quad \omega_1 = 0.1281 \text{ rad/s} \\ \omega_h &= 11.45 \text{ rad/s}, \quad \omega'_2 = 0.2412 \text{ rad/s}, \quad \omega_2 = 0.5153 \text{ rad/s} \\ \omega_{1,\text{nom}} &= 0.0383 \text{ rad/s}, \quad \omega'_3 = 0.9703 \text{ rad/s}, \quad \omega_3 = 2.073 \text{ rad/s} \\ \omega_{2,\text{nom}} &= 277 \text{ rad/s}, \quad \omega'_4 = 3.904 \text{ rad/s}, \quad \omega_4 = 8.341 \text{ rad/s}. \end{aligned} \quad (81)$$

V. PERFORMANCE ANALYSIS

The performance analysis is performed for all three controllers in the frequency domain with the linear model and in the time domain with the nonlinear model. Two operating points are selected: The first one is for nominal conditions ($M_t = 600 \text{ kg}$, $\mu = 1$, and $V_{\text{xref}} = 70 \text{ km/h}$) and the second one for extreme conditions ($M_t = 900 \text{ kg}$, $\mu = 0.4$, and $V_{\text{xref}} = 90 \text{ km/h}$).

Fig. 12 presents the Bode plots of the PI controller, the Hinf controller, and the CRONE controller. Fig. 13 presents the open-loop Bode plots obtained with the PI controller [see Fig. 13(a)], the Hinf controller [see Fig. 14(b)], and the CRONE controller [see Fig. 13(c)] around the first (in dashed blue: nominal) and second (in solid red: extreme) operating points. Fig. 14 shows the open-loop Nichols obtained with the PI controller [see Fig. 14(a)], the Hinf controller [see Fig. 14(b)],

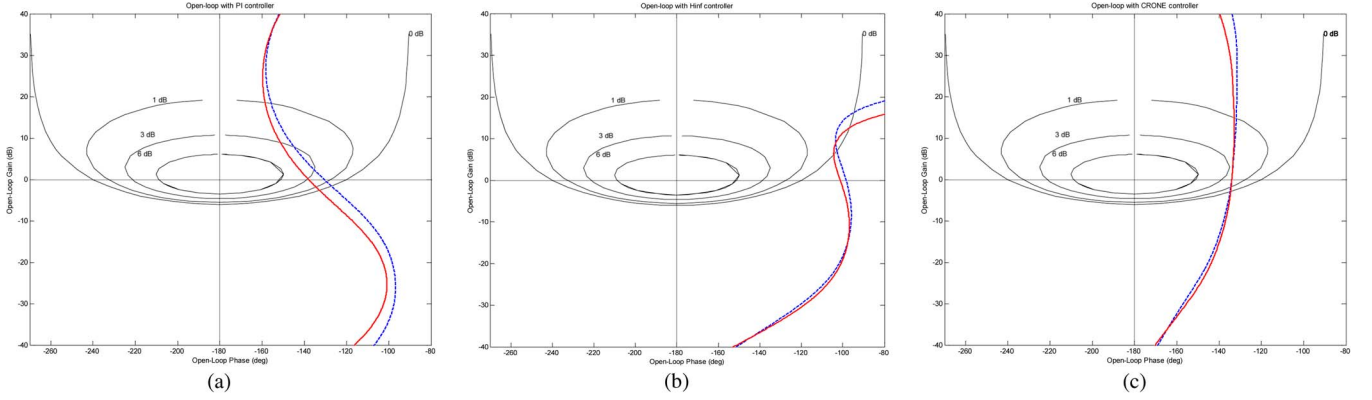


Fig. 14. Open-loop Nichols loci obtained with the (a) PI controller, the (b) Hinf controller, and the (c) CRONE controller.

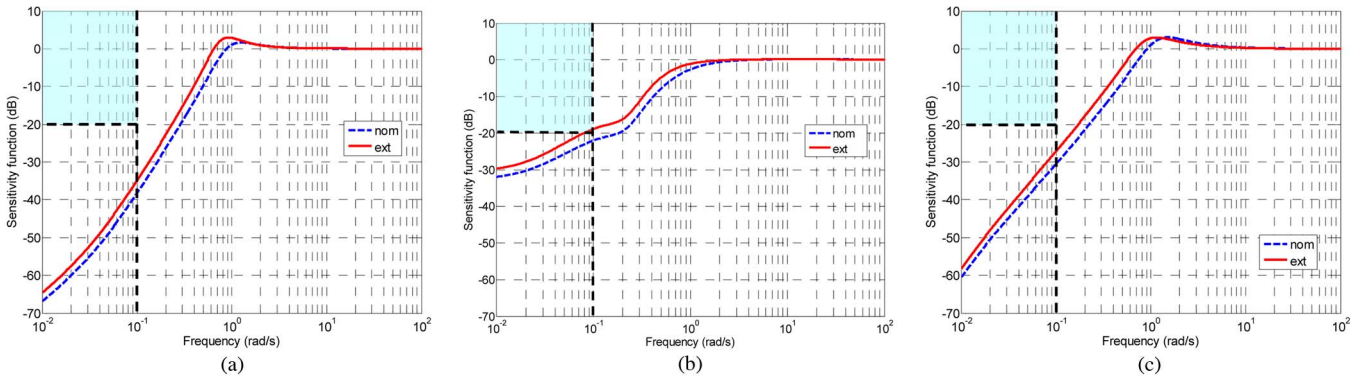


Fig. 15. Sensitivity functions with the (a) PI controller, the (b) Hinf controller, and the (c) CRONE controller.

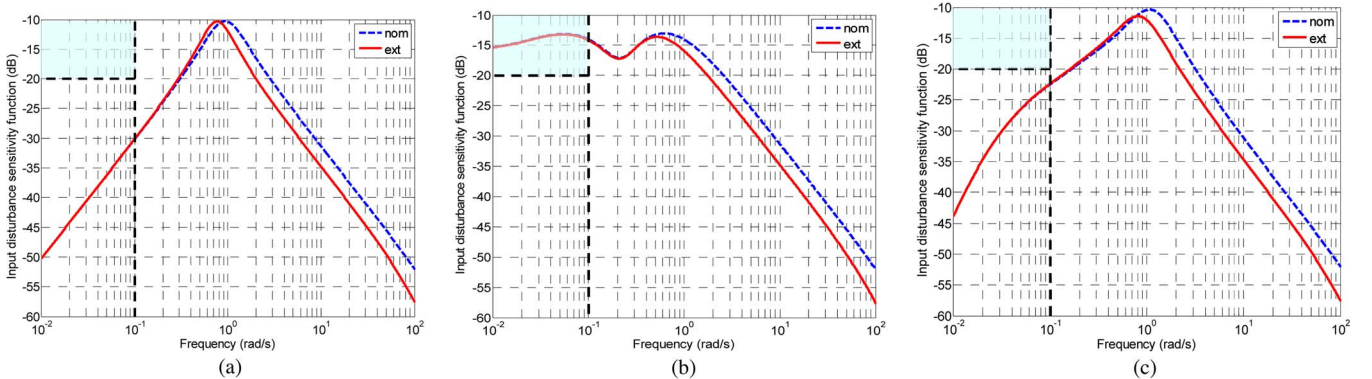


Fig. 16. Input disturbance sensitivity functions with the (a) PI controller, the (b) Hinf controller, and the (c) CRONE controller.

and the CRONE controller [see Fig. 14(c)] around the first and second operating points. With the CRONE controller, the phase margin (45°) remains constant for the extreme values, illustrating the stability degree robustness versus gain uncertainties in the frequency domain.

Figs. 15–18 present the different sensitivity functions obtained with the PI controller, the Hinf controller, and the CRONE controller around the operating points along with the associated constraints in black dashed lines and blue zones. For the nominal operating point (in dashed blue), all performance bounds are respected with the PI and CRONE controllers. For both operating points, the Hinf controller cannot respect the

constraints fixed for the level of rejection of the input perturbation [see Fig. 16(b)] and for the input sensitivity function [see Fig. 18(b)]. For the extreme operating point (in solid red), all performance bounds are respected with CRONE controllers, which is not the case for the stability degree obtained with the PI controller [see Fig. 17(a)] and for the sensitivity function obtained with the Hinf controller [see Fig. 15(b)].

Fig. 19 shows the closed-loop step responses obtained with the PI controller [see Fig. 19(a)], the Hinf controller [see Fig. 19(b)], and the CRONE controller [see Fig. 19(c)] around the operating points. With the CRONE and Hinf controllers, the first overshoot and the damping remain constant for the extreme

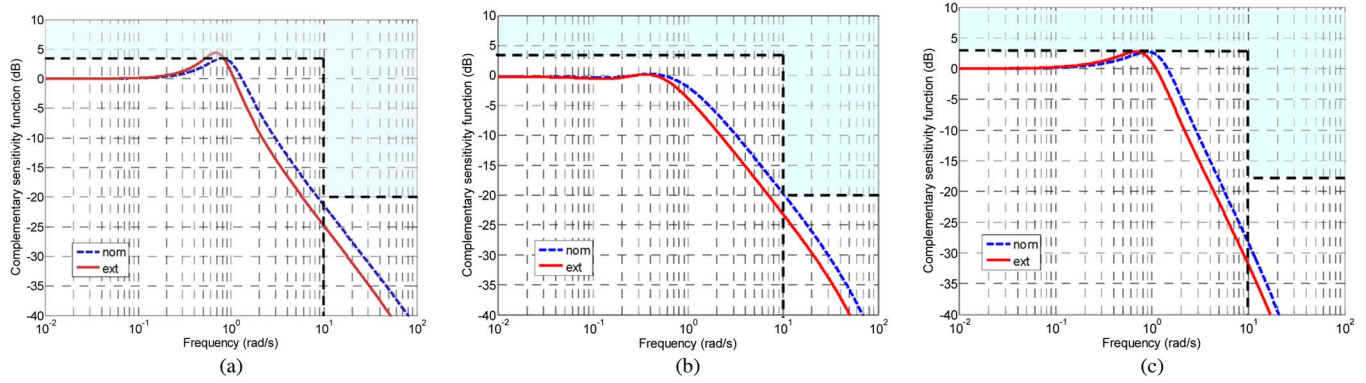


Fig. 17. Complementary sensitivity functions with the (a) PI controller, the (b) Hinf controller, and the (c) CRONE controller.

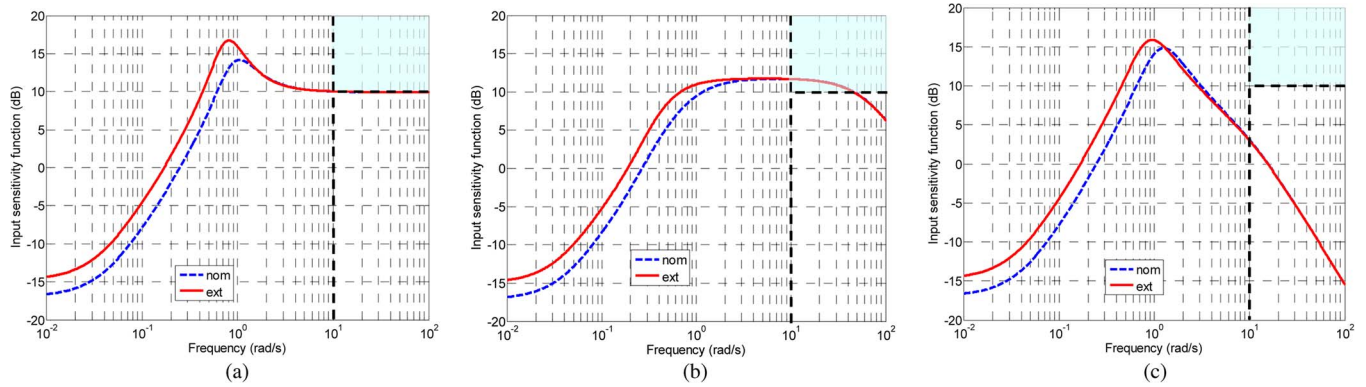


Fig. 18. Input sensitivity functions with the (a) PI controller, the (b) Hinf controller, and the (c) CRONE controller.

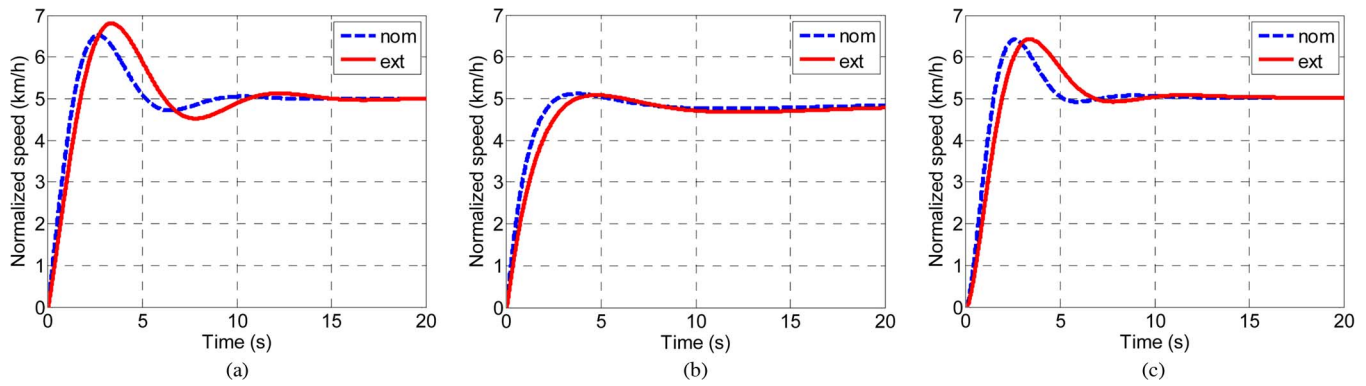


Fig. 19. Normalized step responses with the (a) PI controller, the (b) Hinf controller, and the (c) CRONE controller.

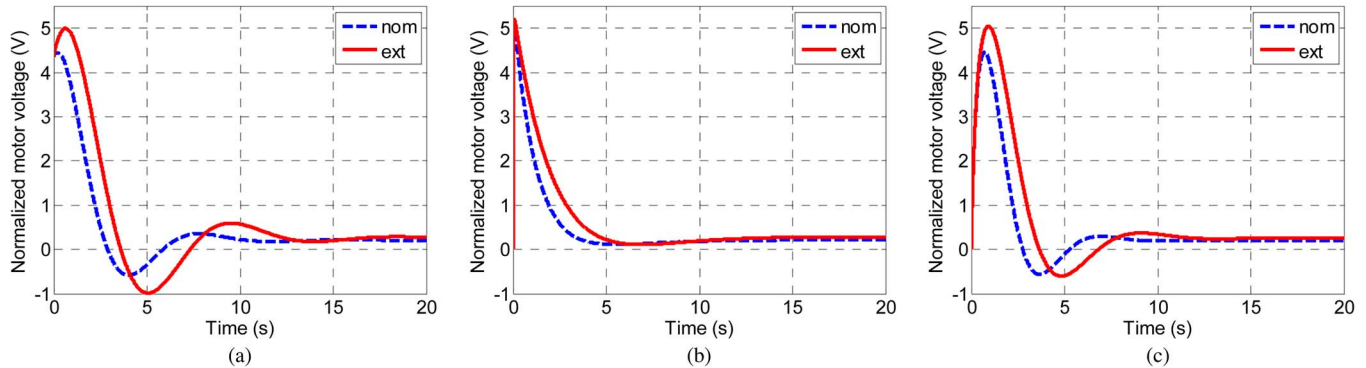


Fig. 20. Normalized control signal responses in rejection mode with the (a) PI controller, the (b) Hinf controller, and the (c) CRONE controller.

values, illustrating the stability degree robustness versus gain uncertainties in time domain. The command signals are also presented in Fig. 20.

Robustness leads to a constant first overshoot with the CRONE controller in spite of variation of the plant parameters, as shown in Fig. 19(c).

This behavior can also be observed through analysis of the closed-loop damping ratio. By taking into account the dynamic decoupling between the two modes of $G(s)$ ($\omega_2/\omega_1 \approx 10^4$) and because $\omega_2 \gg \omega_u$ ($\omega_2/\omega_u \approx 2 \cdot 10^2$), the expression of $G(s)$ can be simplified as follows:

$$G(s) = \frac{V_x(s)}{U_c(s)} \bigg|_{\substack{\alpha_r=0 \\ f_{0x}=0}} \approx \frac{G_0}{\frac{s}{\omega_1} + 1}. \quad (82)$$

The complementary sensitivity function $T_{PI}(s)$ obtained using the PI controller (61) is then given as follows:

$$T_{PI}(s) = \frac{C_{PI}(s)G(s)}{1 + C_{PI}(s)G(s)} = \frac{1 + \frac{s}{\omega_i}}{1 + 2\zeta_{BF}\frac{s}{\omega_{BF}} + \left(\frac{s}{\omega_{BF}}\right)^2} \quad (83)$$

where

$$\begin{cases} \omega_{BF} = \sqrt{C_{0PI}G_0\omega_i\omega_1} \\ \zeta_{BF} = \frac{1}{2} \left(\frac{1+C_{0PI}G_0}{C_{0PI}G_0} \right) \sqrt{\frac{C_{0PI}G_0\omega_1}{\omega_i}}. \end{cases} \quad (84)$$

Replacing ω_1 by (33) and G_0 by (35) and considering $C_{0PI}G_0 \gg 1$ give

$$\begin{cases} \omega_{BF} \approx \sqrt{C_{0PI}\omega_i \frac{2K_A K_T}{r_0 M_t}} \\ \zeta_{BF} \approx \frac{1}{2} \sqrt{\frac{C_{0PI}}{\omega_i} \frac{2K_A K_T}{r_0 M_t}}. \end{cases} \quad (85)$$

In this case, the resulting damping ratio ζ_{BF} is a function of the mass, in such a way that, when the mass M_t increases, the damping ratio ζ_{BF} decreases.

However, using a second generation CRONE control, the damping ratio depends only on the chosen fractional order n , such that

$$\zeta(n) = -\cos\left(\frac{\pi}{n}\right) = 0.5 \quad \text{with } n = 1.5. \quad (86)$$

This characteristic of the CRONE control was already used to design the CRONE suspension [17].

Simulations have been performed using the validation model of the car, with three controllers. Starting at nominal velocity (70 km/h), a rectangular pulse of 700 N with a duration of 2 s simulating a wind gust is applied at $t = 5$ s. Fig. 21 presents the vehicle velocity and the control signal in rejection mode obtained without controller (a, e), with the PI controller (b, f), with the Hinf controller (c, g), and with the CRONE controller (d, h) around the nominal (in dashed blue) and extreme (in red) operating points. One can note that the control signal remains smaller than the saturation value (+12 V). Simulation results

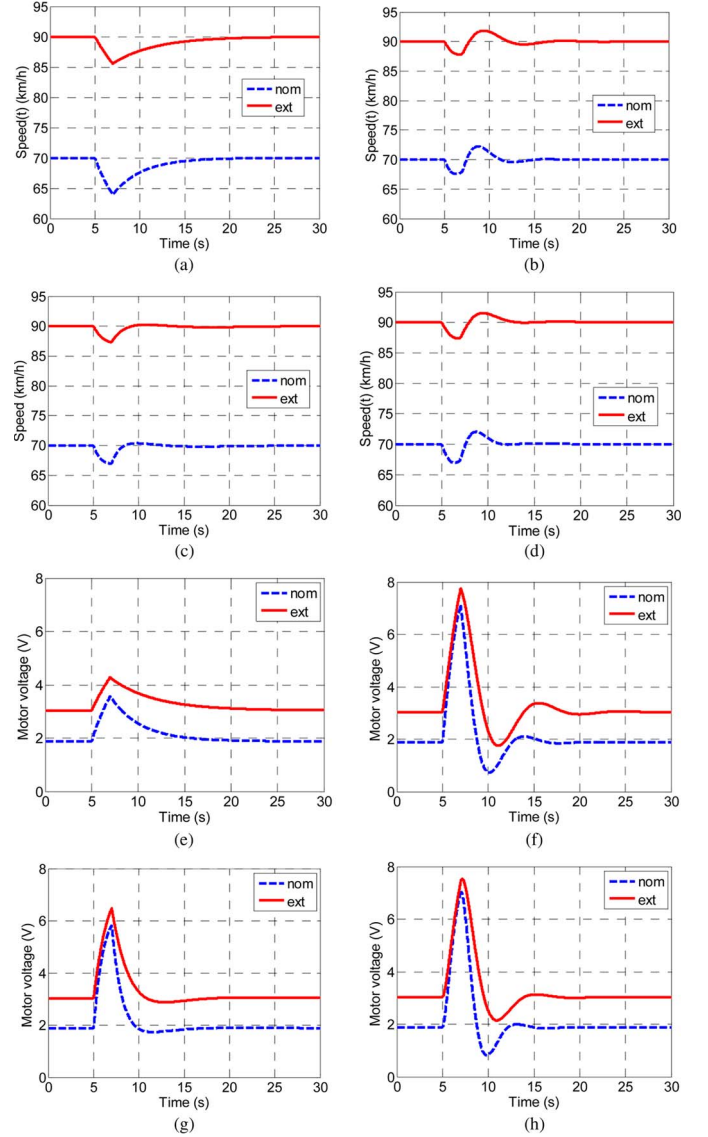


Fig. 21. (a)–(d) Velocity responses and (e)–(h) Control efforts (first column: without controller; second: PI; third: Hinf; fourth: CRONE).

are similar to those obtained with linear model, which means the linear model is valid.

VI. CONCLUSION

In this paper, a comparison between PI, Hinf, and CRONE controllers for the design of a car CC system has been proposed. Synthesis of the controllers is performed after linearization of the vehicle model presented in Section III. Due to the system characteristics (almost constant phase around the open-loop crossover frequency) and the desired specifications, the second generation of CRONE control appears to be well suited. Simulations obtained with the nonlinear vehicle model confirm better results in terms of robustness to mass and velocity uncertainties with the CRONE approach.

Future work will be oriented to the extension of the approach proposed in this paper to the design of an entire ADAS system taking into account not only longitudinal but lateral dynamics as well.

REFERENCES

- [1] J. P. Kreiss, L. Schüler, and K. Langwieder, "The effectiveness of primary safety features in passenger cars in Germany," presented at the 19th Int. Technical Conf. Enhanced Safety Vehicles, Washington, DC, USA, Jun. 6–9, 2005, Paper 05-0145.
- [2] J. Broughton, "The benefits of improved car secondary safety," *Accident Anal. Prevent.*, vol. 35, no. 4, pp. 527–535, Jul. 2003.
- [3] S. Ishida and J. E. Gayko, "Development, evaluation and introduction of a lane keeping assistance system," in *Proc. IEEE Intell. Veh. Symp.*, Jun. 2004, pp. 943–944.
- [4] A. Vahidi and A. Eskandarian, "Research advances in intelligent collision avoidance and adaptive cruise control," *IEEE Trans. Intell. Transp. Syst.*, vol. 4, no. 3, pp. 143–153, Sep. 2003.
- [5] A. Miller *et al.*, "Euro Ncap Rating Review," Euro NCAP, Brussels, Belgium, Tech. Rep., Jul. 2013.
- [6] L. Iftekhar and R. Olfati-Saber, "Autonomous driving for vehicular networks with nonlinear dynamics," in *Proc. IEEE IV*, Jun. 2012, pp. 723–729.
- [7] D. E. Chang, S. C. Shadden, J. E. Marsden, and R. Olfati-Saber, "Collision avoidance for multiple agent systems," in *Proc. 42nd IEEE Conf. Decision Control*, Dec. 2003, vol. 1, pp. 539–543.
- [8] H. T. Zhang, C. Zhai, and Z. Chen, "A general alignment repulsion algorithm for flocking of multi-agent systems," *IEEE Trans. Autom. Control*, vol. 56, no. 2, pp. 430–435, Feb. 2011.
- [9] C. W. Reynolds, "Flocks, herds and schools: A distributed behavioral model," *ACM SIGGRAPH Comput. Graphics*, vol. 21, no. 4, pp. 25–34, Jul. 1987.
- [10] R. Olfati-Saber and R. M. Murray, "Distributed cooperative control of multiple vehicle formations using structural potential functions," in *Proc. IFAC World Congr.*, 2002, pp. 346–352.
- [11] H. Suzuki and T. Nakatsuji, "Effect of adaptive cruise control (acc) on traffic throughput: Numerical example on actual freeway corridor," *JSAE Rev.*, vol. 24, no. 4, pp. 403–410, Oct. 2003.
- [12] A. Morand, X. Moreau, P. Melchior, and M. Moze, "Robust cruise control using crone approach," *Fract. Different. Appl.*, vol. 6, pp. 468–473, 2013.
- [13] A. Khodayari, A. Ghaffari, S. Ameli, and J. Flahatgar, "A historical review on lateral and longitudinal control of autonomous vehicle motions," in *Proc. 2nd ICMET*, Sep. 2010, pp. 421–429.
- [14] T. J. Ren, T. C. Chen, and C. J. Chen, "Motion control for a two-wheeled vehicle using a self-tuning PID controller," *Control Eng. Pract.*, vol. 16, no. 3, pp. 365–375, Mar. 2008.
- [15] L. Nouveliere and S. I. Mammar, "Experimental vehicle longitudinal control using a second order sliding mode technique," *Control Eng. Pract.*, vol. 15, no. 8, pp. 943–954, Aug. 2007.
- [16] R. A. Z. Daou, X. Moreau, and C. Francis, "Effect of hydropneumatic components nonlinearities on the crone suspension," *IEEE Trans. Veh. Technol.*, vol. 61, no. 2, pp. 466–474, Feb. 2012.
- [17] A. Oustaloup, X. Moreau, and M. Nouillant, "From fractal robustness to non-integer approach in vibration insulation: The crone suspension," in *Proc. 36th IEEE Conf. Decision Control*, Dec. 1997, vol. 5, pp. 4979–4984.
- [18] A. Oustaloup, B. Mathieu, and P. Lanusse, "The CRONE control of resonant plants: Application to a flexible transmission," *Eur. J. Control*, vol. 1, no. 2, pp. 113–121, 1995.
- [19] A. Oustaloup, J. Sabatier, and P. Lanusse, "From fractal robustness to crone control," *Fraction. Calculus Appl. Anal.*, vol. 2, no. 1, pp. 1–30, 1999.
- [20] V. Pommier, J. Sabatier, P. Lanusse, and A. Oustaloup, "Crone control of a nonlinear hydraulic actuator," *Control Eng. Pract.*, vol. 10, no. 4, pp. 391–402, Apr. 2002.
- [21] G. Colin *et al.*, "Multi-siso robust crone design for the air path control of a diesel engine," in *Proc. IFAC World Congr.*, 2011, pp. 2254–2259.
- [22] B. Feytout, P. Lanusse, J. Sabatier, and S. Gracia, "Robust crone design for a variable ratio planetary gearing in a variable speed wind turbine," *Asian J. Control*, vol. 15, no. 3, pp. 806–818, May 2013.
- [23] J. Sabatier *et al.*, "Fractional system identification for lead acid battery state of charge estimation," *Signal Process.*, vol. 86, no. 10, pp. 2645–2657, Oct. 2006. Special Section: Fractional Calculus Applications in Signals and Systems.
- [24] X. Moreau, C. Ramus-Serment, and A. Oustaloup, "Fractional differentiation in passive vibration control," *Nonlinear Dynam.*, vol. 29, no. 1–4, pp. 343–362, Jul. 2002.
- [25] C. Nouillant, F. Assadian, X. Moreau, and A. Oustaloup, "Feedforward and crone feedback control strategies for automobile abs," *Veh. Syst. Dynam.*, vol. 38, no. 4, pp. 293–315, Oct. 2002.
- [26] C. Nouillant, F. Assadian, X. Moreau, and A. Oustaloup, "A cooperative control for car suspension and brake systems," *Int. J. Automot. Technol.*, vol. 3, no. 4, pp. 147–155, 2002.
- [27] P. Serrier, X. Moreau, J. Sabatier, and A. Oustaloup, "Taking into account of nonlinearities in the crone approach: Application to vibration isolation," in *Proc. 32nd IEEE IECON/IECON*, Nov. 2006, pp. 5360–5365.
- [28] P. Serrier, X. Moreau, and A. Oustaloup, "Volterra series based analysis of components nonlinearities in a limited-bandwidth fractional differentiator achieved in hydropneumatic technology," in *Proc. 2nd IFAC Workshop FDA*, 2006, pp. 475–480.
- [29] C. Espanet *et al.*, "In-wheel motor for a small hybrid electric vehicle: design, realization and experimental characterization," in *Proc. IEEE ECCE*, 2012, pp. 892–898.
- [30] T. D. Gillespie, *Fundamentals of Vehicle Dynamics*. Warrendale, PA, USA: Soc. Automot. Eng., 1992, vol. 400.
- [31] H. B. Pacejka and I. J. M. Besselink, "Magic formula tyre model with transient properties," *Veh. Syst. Dynam.*, vol. 27, no. S1, pp. 234–249, 1997.
- [32] P. Lanusse, A. Oustaloup, and J. Sabatier, "Step-by-step presentation of a 3rd generation crone controller design with an anti-windup system," in *Proc. ENOC*, Eindhoven, The Netherlands, 2005, pp. 7–12.
- [33] A. Oustaloup, B. Mathieu, and P. Lanusse, "Second generation crone control," in *Proc. Int. Conf. Syst., Man Cybern., Syst. Eng. Serv. Humans*, Oct. 1993, vol. 2, pp. 136–142.
- [34] A. Oustaloup, P. Melchior, P. Lanusse, O. Cois, and F. Dancla, "The crone toolbox for matlab," in *Proc. IEEE Int. Symp. CACSD*, 2000, pp. 190–195.
- [35] R. Malti, P. Melchior, P. Lanusse, A. Oustaloup, "Towards an object oriented crone toolbox for fractional differential systems," in *Proc. 18th IFAC World Congr.*, 2011, pp. 10 830–10 835.
- [36] Crone Toolbox-Official Website. [Online]. Available: www.ims-bordeaux.fr/CRONE/toolbox/
- [37] P. Lanusse, R. Malti, and P. Melchior, "Crone control system design toolbox for the control engineering community: Tutorial and case study," *Philos. Trans. Roy. Soc. A, Math., Phys. Eng. Sci.*, vol. 371, no. 1990, May 2013.
- [38] A. Oustaloup, B. Mathieu, and P. Lanusse, "Complex non-integer integration contours of isoamortissement," *Eur. J. Autom. Syst.*, vol. 29, no. 1, pp. 177–202, 1995.
- [39] P. Lanusse, H. Benlaoukli, D. Nelson-Gruel, and A. Oustaloup, "Fractional-order control and interval analysis of siso systems with time-delayed state," *IET Control Theory Appl.*, vol. 2, no. 1, pp. 16–23, Jan. 2008.
- [40] A. Oustaloup, P. Lanusse, J. Sabatier, and P. Melchior, "Crone control: Principles, extensions and applications," *J. Appl. Nonlinear Dynam.*, vol. 2, no. 3, pp. 207–223, 2013.



Audrey Morand was born in Nantes, France, in 1988. She received the Master's degree in intelligent systems from Pierre and Marie Curie University, Paris, France, in 2011 and the Ph.D. degree in control engineering from the University of Bordeaux, Talence, France, in 2014.

She is currently with the University of Bordeaux and with PSA Peugeot Citroën, Vélizy-Villacoublay, France, as a Research Engineer, specializing in advanced driver-assistance systems.



Xavier Moreau was born in France on March 23, 1966. He received the Ph.D. degree in control engineering and the Accreditation to supervise research (HDR) from the University of Bordeaux, Talence, France, in 1995 and 2003, respectively.

He is currently a Professor with the Department of Sciences and Technologies, University of Bordeaux, as well as with OpenLab PSA-IMS "Electronics and Systems for Automotive," Talence. His research interests include fractional differentiation and its applications in engineering sciences and, more particularly, in vibration control, vehicle dynamics, global chassis control, and advanced driver-assistance systems.

Dr. Moreau received the AFCET Trophy for the CRONE suspension in 1995.



Pierre Melchior was born in France on 1961. He graduated from the University of Bordeaux, Talence, France, and received the Ph.D. degree in control engineering from Paul Sabatier University, Toulouse, France, in 1989 and the Accreditation to supervise research (HDR) from the University of Bordeaux, in 2014.

He is currently an Associate Professor of control theory and a Researcher with Laboratory IMS, University of Bordeaux, and OpenLab PSA-IMS "Electronics and Systems for Automotive," Talence. He is Comanager of the CRONE team. His research interests include systems, control theory, robotics, and biomechanics (e.g., fractional systems, fractional path planning, fractional motion planning, and muscle modeling).



Franck Guillemard was born in France on March 18, 1968. He received the Ph.D. degree in control engineering from the University of Lille, Villeneuve-d'Ascq, France, in 1996.

He is currently with the Scientific Department, PSA Peugeot Citroën, Vélizy-Villacoublay, France, where he is in charge of advanced research concerning computing science, electronics, photonics, and control. He is also with the OpenLab PSA-IMS "Electronics and Systems for Automotive," Talence, France. His research interests include modeling, design, and control of mechatronic systems for automotive applications.



Mathieu Moze was born in Bordeaux, France, on 1979. He received the M.Eng. degree in mechatronics from French Ecole Nationale d'Ingenieurs (ENIT), Tarbes, France, and the M.S. degree in control systems from Institut National Polytechnique Toulouse, Toulouse, France, both in 2003, and the Ph.D. degree in control theory from the University of Bordeaux, Talence, France, in 2007.

In 2008, he became a Consultant to a number of industrial firms and was associated with the OpenLab PSA-IMS "Electronics and Systems for Automotive," Talence, where he studied algebraic approaches to fractional order systems analysis and robust control theory. Since 2010, he has been with the Scientific Department, PSA Peugeot Citroën, Vélizy-Villacoublay, France, where he conducts advanced research concerning the modeling, design, and control of mechatronic systems for automotive applications.